Contents lists available at ScienceDirect

Chinese Chemical Letters

journal homepage: www.elsevier.com/locate/cclet

Rational design of self-sacrificial template derived *quasi*-Cu-MOF composite as anodes for high-performance lithium-ion batteries

Jiajing Wang, Xiaotian Guo, Qingling Jing, Wenting Li, Tingting Chen, Rongmei Zhu, Huan Pang*

School of Chemistry and Chemical Engineering, Yangzhou University, Yangzhou 225000, China

ARTICLE INFO

Article history:
Received 22 May 2022
Revised 2 July 2022
Accepted 12 July 2022
Available online 19 July 2022

Keywords:
Quasi-MOF
Conductivity
Porous structure
Anode
Lithium-ion batteries

ABSTRACT

MOF-based composites have aroused widespread concern due to their controllable morphology and pore characteristics. Nevertheless, the poor conductivity and volume expansion hinder its practical application in LIBs. Herein a classical structure HKUST-1, as the precursor, was used to fabricate *quasi*-Cu-MOF composite through a facile thermal decomposition strategy. The results showed that *quasi*-Cu-MOF composite had superior reversible specific capacity (627.5 mAh/g at 100 mA/g) and outstanding cycle stability (514.6 mAh/g at 500 mA/g after 400 cycles) as anodes for LIBs. The results demonstrated that the low-temperature calcination strategy played a significant role in morphology retaining during cycling and the derived copper framework play a crucial part in conductivity improvement. This work is helpful to the design of high-performance electrodes with advanced three-dimensional hierarchical structures.

© 2023 Published by Elsevier B.V. on behalf of Chinese Chemical Society and Institute of Materia Medica, Chinese Academy of Medical Sciences.

Existing fossil fuels such as petroleum, coal, and other products that are in a highly depleted state have limited stocks, and the old energy supply model is unsustainable imminent [1–3]. In addition, challenges such as population growth, rapid urbanization and industrial modernization propel rapid developments of new environmentally friendly energy sources [4–6]. Metal-organic framework (MOF), namely porous coordination polymer (PCP), is a highly crystalline material with a periodic network structure composed of the junction between metal ions and groups with organic ligands through coordination bonds [7]. Due to the unique construction, MOF has many advantages, such as porosity, high specific surface area (SSA), regular pore size and controllable structure, making it a universal template or media for preparing other porous materials. Battery research is in full swing, and MOF-based materials with such advantages attract many researchers' attention. The synthetic method and structural design of MOF have been the focus of current researchers [8–10]. Nowadays, MOF is widespread used in a variety of fields [11–15].

However, the three-dimensional (3D) network structure of MOF always caves during the conversion to active materials or the cycling process in the application process. It is significant to preserve the 3D framework while generating active species for the comprehensive application of MOF [16]. The controllable structural damage caused by MOF annealing can assemble a new generation of materials with low crystallinity but particular properties [17,18]. Structural defects may lead to unsaturated coordination sites around metal ions, which is beneficial to enhancing reactivity and increasing porosity [19,20]. The reasonable selection of the suitable decomposition temperature can lead to partial pyrolysis of the frame structure and ensure that the remaining materials maintain the original morphology and porosity. Notably, Xu's group [21] proposed the new concept of *quasi*-MOF to comprehend both a strong interaction and a porous structure with a synergetic effect between the stationary metal nanoparticles and the inorganic nodes. *Quasi*-MOF is developed by controlling partial deligandation of MOF to generate Lewis acid centres, which enhance the accessibility of M-O sites while maintaining structural characteristics [22]. With the formation of hierarchical micropores and mesopores, the intrinsic specific surface area is preserved or increased upon partial deligandation, facilitating the diffusion of the electrolyte to and from the active centres of products [23]. *Quasi*-MOF can represent an intermediate state between highly crystalline MOF materials and metal compounds, their properties attracting more and more attention.

Tsumori *et al.* [21] used the impregnation method to introduce Au nanoparticles into Cr-MIL-101, and then thermally induced deligandation to form *quasi*-MIL-101 with accessible Cr-O sites for low-temperature CO oxidation. It not only preserves the framework structure with plenty of functional groups from the original MOF but also possesses highly active and stable metal/metal

---

* Corresponding author.
E-mail address: panghuan@yzu.edu.cn (H. Pang).

https://doi.org/10.1016/j.cclet.2022.07.018

1001-8417/© 2023 Published by Elsevier B.V. on behalf of Chinese Chemical Society and Institute of Materia Medica, Chinese Academy of Medical Sciences.

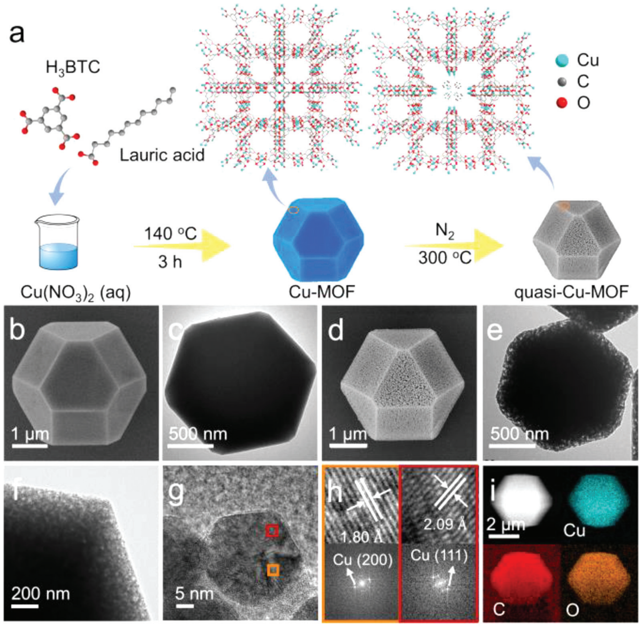

Fig. 1. (a) Schematic diagram of the growth process and architecture of *quasi*-Cu-MOF composite. (b) SEM and (c) TEM images of $[Cu_3(btc)_2]_n$. Morphology characterization of *quasi*-Cu-MOF composite. (d) SEM, (e) TEM, (f, g) HRTEM images, (h) lattice images, (i) HAADF-STEM image and corresponding elemental mapping images.

oxide species. Bagheri *et al.* further confirmed this controllable de-coordination strategy [24]. Experimental results prove that controlled pyrolysis can generate highly active Lewis acid sites within *quasi*-HKUST. Meanwhile, the material's porosity and framework structure remain intact, ensuring that reactants can access active sites and provide space for the diffusion of reagents and products. Cui *et al.* [25] fabricated Co/MnO_x@*quasi*-MOF-74 catalyst with a core-shell structure. The Co^0 nanoparticles generated from MOF-74 became new active centres during the heat treatment process, and the uniformly dispersed Co^{2+} unsaturated coordination centres and Co_2C synergized to strengthen the CO insertion process, which showed impressive performance in the CO hydrogenation process. Using Ni-BDC as a template, Ni_2P@*quasi*-Ni-BDC composites were prepared by partial deligandation and phosphorization processes, which retained their inherent electrochemical activity and exhibited excellent synergistic effects in electrochemical applications [26]. From the reports above, *quasi*-MOF composites have been used in the field of catalysis [27,28] but have not been reported as anodes for LIBs.

As one of the most intensely studied MOFs, HKUST-1 has shown remarkable performance which is considered feasible to apply in actual applications, mainly adsorption and separation, catalyst, sensor [29]. Herein, we choose it as the precursor and porous *quasi*-MOF composite was obtained by low-temperature calcination strategy using it as a template. In this study, the favourable morphology and mesoporous structure provided by pristine Cu-MOF are beneficial for electrolyte diffusion and Li^+ ions storage. The nano-scale copper particles partially occupy part of the original MOF cavity *in situ* through the annealing treatment, and the formed conductive framework plays a crucial part in improving the conductivity and alleviating the expansion during cycling. The results show that *quasi*-Cu-MOF composite as the LIBs anode has an impressive reversible capacity (627.5 mAh/g at 100 mA/g) and superior cycle stability.

Fig. 1a illustrates the synthesis process of *quasi*-Cu-MOF composite. Firstly, $[Cu_3(btc)_2]_n$ polyhedron was prepared by solvothermal reaction of $Cu(NO_3)_2 \cdot 3H_2O$ and 1,3,5-benzenetricarboxylic acid. Then, a series of derivatives were obtained by one-step calcination with $[Cu_3(btc)_2]_n$ as the precursor. The low magnification SEM image clearly shows that the precursor $[Cu_3(btc)_2]_n$ is a cuboctahedron with a size of 2–3 µm (Figs. 1b and c). According to the TG curve (Fig. 2a), we selected 250, 300 and 350 °C as the calcination temperature of this experiment to obtain different MOF derivatives and named M1, M2 and M3. As expected, the three-dimensional structure remained well after calcination. In SEM images with higher magnification (Figs. 1d and e, Fig. S1 in Supporting information), the smooth surface of M2 is rough and appeared obvious pores, while the morphology of M1 is similar to that of the precursor, and the exterior of M3 is jumbled coated with precipitates. As shown in Figs. 1f and g, the copper nanoparticles are well dispersed in the pristine Cu-MOF framework and the sizes of copper nanoparticles are rather small with a narrow size distribution (25 ± 5 nm). The EDS element mapping results in Fig. 1i verify the even distribution of Cu, C and O elements in the structure. Interestingly, the lattice fringes with a spacing of 2.09 Å and 1.81 Å correspond to the (111) and (200) crystal planes of metallic copper, respectively (Fig. 1h), indicating that copper particles are closely coupled with MOF structure [30]. The surrounding disordered regions correspond to amorphous carbon and MOF structures. The structural shrinkage is due to thermal stress and decomposition [31]. What's more, there are amorphous outer layers with some cracks on the surface of copper particles, which means that the electrolyte molecules can contact the surface of copper particles without passing through the carbon layer.

There are two obvious cooling zones in the TG curve (Fig. 2a), corresponding to the removal of adsorbed solvent molecules in the channel and the pyrolysis of the organic skeleton. The weight loss ratios corresponding to two processes above were 29.8% and 31.0%, respectively. As is shown in Fig. 2b, the characteristic peaks of pristine Cu-MOF synthesized are consistent with the simulated spectra of Cu-MOF while the characteristic peaks of M1 are also consistent with that, but the intensity reduced due to the decrease of crystallinity [32]. Combined with the TG curve, it can be preliminarily judged that compared with pristine Cu-MOF, copper and carbon components appear in M2. Derived carbon materials can prevent the accumulation of active substances during cycling [33,34]. Furthermore, it is found that metal particles' precipitation under the incomplete decomposition of MOF could improve the electrical conductivity of the material [35,36]. However, it can be seen that 350 °C is the period with the fastest mass loss, the sample is in an unstable state. The XRD pattern of M3 shows that the structure of pristine Cu-MOF has changed, and there is a phase transition leading to the formation of metallic copper. The precursor was completely reduced to copper when the calcination temperature was 400 °C (Fig. S2 in Supporting information).

To further reveal the structural evolution of the samples during the pyrolysis process, the pristine Cu-MOF and its derivatives were characterized by FT-IR (Fig. 2c). The alike positions of the main peaks of the M1 and pristine Cu-MOF indicate that they have a similar surface chemistry environment. The bands at 1106 cm^{-1} indicate stretching vibrations of C-O-Cu bonds, and the bands at 761 and 728 cm^{-1} can be ascribed to copper substitution in phenyl. FT-IR spectra show that there is an extensive decarboxylation process at $250 \sim 350$ °C. With the increase of temperature, the infrared peak corresponding to the O-C=O functional group at $1300 \sim 1700$ cm^{-1} gradually broadened, which confirmed the partial decoupling of the organic ligand skeleton. The aromatic group characteristic signal of M2 appeared at 1595 and 1440 cm^{-1}, respectively [37]. Meanwhile, the vibration characteristic peak of the outer ring C=C at 980 cm^{-1} moderately decreases and disappears [38,39]. At 1670 cm^{-1}, an obvious C=O vibration band also appeared, which was consistent with TG results, implying that the

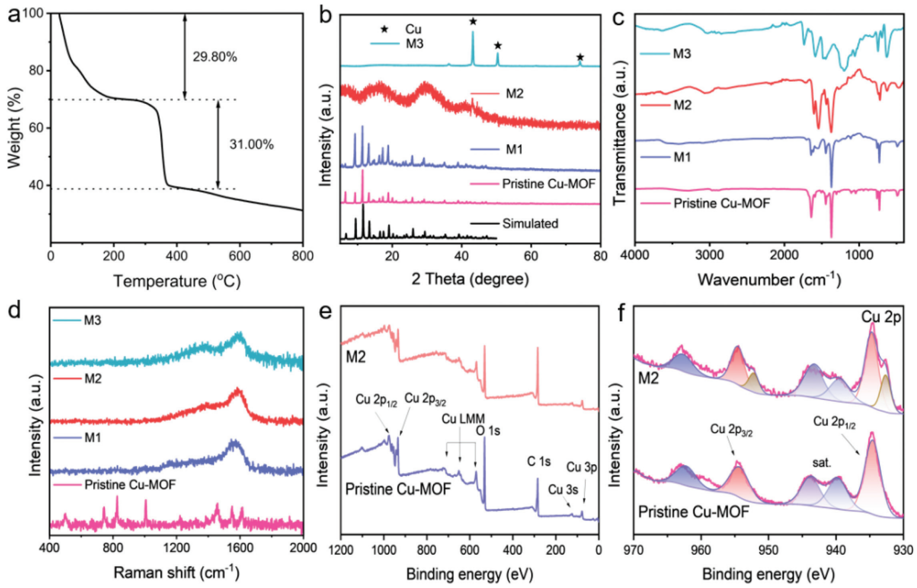

Fig. 2. (a) TGA curve of $[Cu_3(btc)_2]_n$. (b) XRD patterns, (c) FT-IR spectra and (d) Raman spectra of pristine Cu-MOF and its derivatives. (e) XPS survey spectra of pristine Cu-MOF and M2 and high-resolution (f) Cu 2p.

crosslinking pathway of organic residues is changed under pyrolysis conditions.

For comparison, the surface structure and carbon component of samples were studied by Raman spectra (Fig. 2d). Except pristine Cu-MOF, typical carbon signals with a wide defect band can be observed in M1, M2 and M3. The peaks at 1378 cm^{-1} and 1588 cm^{-1} are relevant to the D-band and G-band, respectively. The former represents defects or amorphous properties, and the latter represents the ordered graphitized sp^2 type carbon [40]. Through the strength ratio (I_D/I_G) and wide defect band characteristics, it can be judged that the main carbon component in the sample is mainly amorphous carbon [41]. This result is in good agreement with the experimental results that neither interlayer spacing nor lattice fringes of carbon are observed in HRTEM. In Fig. S4 (Supporting information), the hysteresis loop of P/P_0 near 0.8 can be seen, that is, there is a difference between adsorption and desorption curves. The N_2 adsorption and desorption curves conform to type IV physical adsorption isotherm as a whole, indicating that the material is mainly the mesoporous structure. The SSA of M2 is as high as 61.22 m^2/g. Through BJH calculation, it is determined that the pore size of the material is concentrated at 16.29 nm and the total pore volume is about 0.3187 cm^3/g. Given the above results, the obtained *quasi*-Cu-MOF composite has a superior SSA and rich porosity, which contribute to the dispersion and exposure of active sites, increase the efficiency of Li$^+$ insertion and deintercalation, supply a convenient diffusion path for Li$^+$ ions and provide sufficient voids to effectively alleviate volume changes, leading to large reversible capacity and robust cycle performance of *quasi*-Cu-MOF composite electrode [42].

The composition and chemical bonding state of *quasi*-Cu-MOF composite were characterized by X-ray photoelectron spectroscopy (XPS) techniques. The peaks at 934.9, 531.6 and 286.5 eV are ascribed to Cu 2p, O 1s and C 1s, respectively (Fig. 2e). From the Cu 2p spectra of pristine Cu-MOF in Fig. 2f, there are two typical peaks at 954.4 and 934.9 eV corresponding to Cu 2p$_{1/2}$ and Cu 2p$_{3/2}$, respectively, assigned to Cu(II), which is located at the centre of the MOF structure. Compare with the pristine Cu-MOF, there are two more peaks at 932.7 and 952.2 eV in M2. What is more, the difference between the two peaks is 19.7 eV which can be attributed to Cu^0 particles [43]. The three peaks (284.8, 286.5 and 288.5 eV) in C 1s spectra (Fig. S3a in Supporting information) could correspond to C-C, C-O and O-C=O of *quasi*-Cu-MOF, respectively. In Fig. S3b (Supporting information), the peak of O-Cu (533.78 eV) of pristine Cu-MOF corresponds to the Cu 2p spectra, indicating the existence of Cu(II). The O 1s characteristics peak of M2 located at 531.6 eV can be assigned to Cu-O species [44,45]. These characteristic peaks of M2 have a slight shift in comparison with pristine Cu-MOF spectrum because of the removal of the solvent.

Owning to the fantastic structural characteristics mentioned above, *quasi*-MOF composites have great significance and application possibility in LIBs. The charge/discharge tests were performed within the voltage range of 0.01–3.0 V *vs.* Li$^+$/Li, with pristine Cu-MOF and derivatives as the anode active material and metallic Li as counter electrode in a half-cell configuration. Cyclic voltammetry tests of *quasi*-Cu-MOF composite at 0.1 mV/s for the initial three cycles were presented in Fig. 3a. In the first cycle, three cathodic peaks at 0.20, 0.73 and 1.12 V were observed. The two cathodic peaks at 0.20 and 1.12 V almost disappeared in the subsequent cycles, assigned to the formation of the decomposition of the carbonate electrolytes and a solid electrolytic interface (SEI) layer [46]. The board peak at 0.73 V can be due to the combined redox behaviour of organic ligands and the reduction of Cu^{2+} to metallic Cu^0 as well as the Li$^+$ ions insertion into the framework [47,48]. For the organic moiety, carboxylates which are weakly electron-withdrawing ligands might act as redox centres [49]. In the second cycle, this board peak was shifted to 0.51 V, possibly corresponding to the multistep insertion of Li$^+$ ions to the conjugated organic moieties [50]. The CV curve of the third cycle almost overlaps with that of the second cycle, indicating that the electrode has superior stability. This is also reflected by observation of nearly identical cyclic voltammograms after 400 cycles (Fig. S9 in Supporting information).

The charge and discharge profiles of the *quasi*-Cu-MOF composite at 100 mA/g for the selected cycles are shown in Fig. 3b. In the first discharge curve, an approximate plateau at 1.5 V followed by a gentle gradient upon further discharge to 0.01 V in keeping with the initial CV test, indicates the Li$^+$ ions insertion process and the reduction of organic linkers [51]. The initial discharge/charge capacities of M2 were 1573.5 and 540.2 mAh/g, respectively, corresponding to a coulombic efficiency (CE) of ~34.3%, which is due to

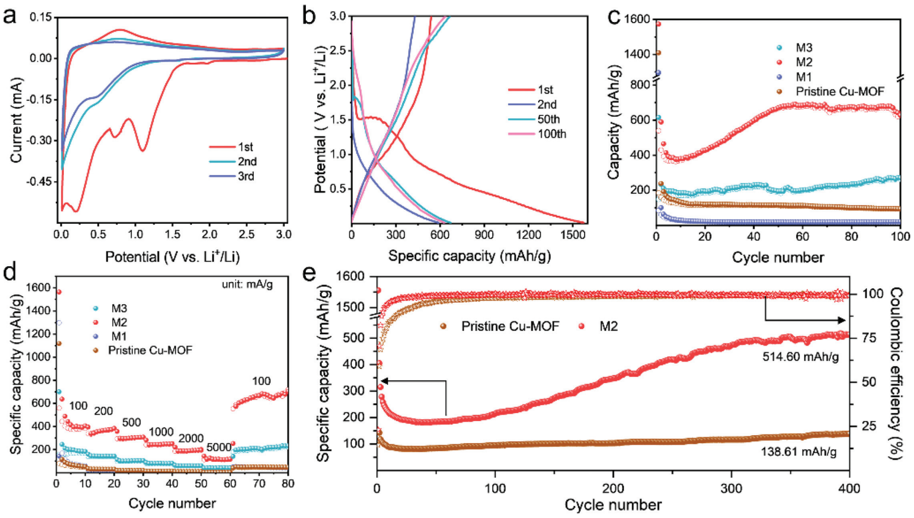

Fig. 3. (a) Cyclic voltammograms, (b) charge/discharge profiles, (c) cycling performance and (d) rate performance at current densities from 100 mA/g to 5000 mA/g of pristine Cu-MOF and its derivatives. (e) Long cycling performance at a current density of 500 mA/g of pristine Cu-MOF and M2.

the existence of guest molecules and many cavities. However, the loss of initial irreversible capacity would be attributed to the formation of SEI film on the electrode surface, the irreversible intercalation of Li^+ and the decomposition of the electrolyte [52]. Worth noting is that the voltage curves after the 50th cycle almost overlap, indicating that it has superior electrochemical reversibility.

Fig. 3c displays the cycling performance of pristine Cu-MOF, M1, M2 and M3 at 100 mA/g. Different from the common anode materials, it is obvious that the discharge capacity of M2 declined during the first several cycles and then slowly increase and remains stable at above 627.5 mAh/g at 100 mA/g after 100 cycles. There is a conspicuous increase in capacity of 1.5 times observed in M2 over 50 cycles, which results from the adsorption of a large number of ions as the electrolyte permeates into the bulk [53]. The increasing specific capacity presented may be in consequence of the sluggish amorphization and equilibration of the *quasi*-Cu-MOF composite electrode [54]. Although the capacity is significantly higher than that of pristine Cu-MOF, the decrease of capacity at the beginning of the cycle is a problem worthy of discussion. If the material is nano-treated [55] or coated with carbon layers [56], it is expected to improve the initial performance of the material as an anode material for LIBs.

Furthermore, the rate-performance of *quasi*-Cu-MOF composite was examined at different current densities varied from 100 mA/g to 5000 mA/g (Fig. 3d). At different high current densities of 100, 200, 500, 1000, 2000, 5000, 100 mA/g, *quasi*-Cu-MOF composite exhibits high capacities of 436.1, 382.3, 308.3, 249.6, 194.9, 118.2, 703.9 mAh/g, respectively. As depicted in Fig. 3e, M2 also shows a good long-term cycling performance (514.6 mAh/g at 500 mA/g after 400 cycles). Under the same conditions, the capacity of pristine Cu-MOF stabilizes at 138.61 mAh/g. The coulombic efficiency of M2 after 400 cycles achieved is as high as ~99%, which demonstrates that M2 delivers a stable reversible capacity for long-term cycling tests. The high SSA and 3D layered network not only facilitate transmission channels for Li^+ ions and electrons but also provide support and relieve the volume expansion during the cycle [57,58]. In addition, the electronic conduction of M2 is significantly improved due to the production of copper and carbon [59,60]. The above results exemplify the superior cycle life and high capacity of *quasi*-Cu-MOF composite, which are of importance to explain the electrochemical behaviour of the electrode material. Some research about similar Cu-based composites for LIBs have been reported previously as shown in Table S1 (Supporting information). It was interesting that the specific capacity and cycling performance of *quasi*-Cu-MOF composite was superior and comparable to the others.

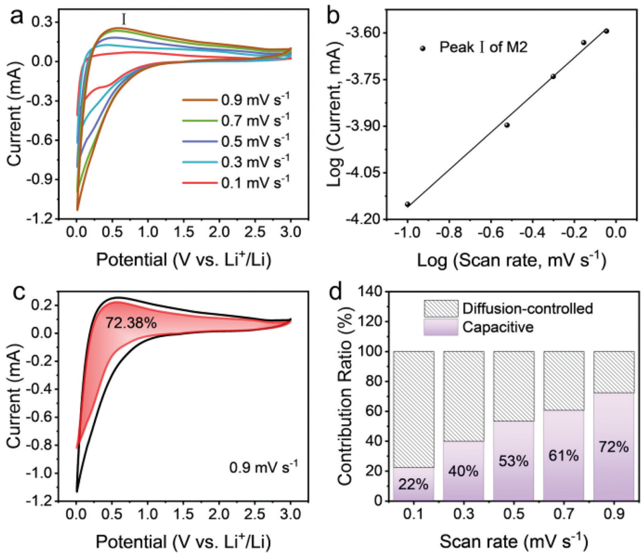

Fig. 4. (a) CV curves at various scan rates (0.1–0.9 mV/s) of M2. (b) Linear relationship between log(i) and log(ν) at the peaks. (c) Normalized contribution ratio of diffusion-controlled and capacitive capacities at 0.9 mV/s. (d) Capacitive contributions scanning at various scan rates, (the shaded area is associated with the pseudocapacitive property).

The capacity contribution of batteries is provided by a combination of capacitive and diffusion processes. To investigate the kinetics of its Li^+ ions storage behaviour, the CV curves of M2 were recorded at various scan rates (0.1–0.9 mV/s), as shown in Fig. 4a. The relationship between the peak current (i) and scan rate (ν) obeys Eq. 1, as shown below:

$$\log(i) = \mathrm{a} + \mathrm{b}\log(\nu) \tag{1}$$

where both a and b are constants. For M2, the value of the slope of the current peak fitting curve is 0.6 (Fig. 4b), implying that the capacity contribution of batteries is a combination of capacitive and diffusion process (namely, $b = 0.5$, diffusion process; $b = 1$, capacitive process; $0.5 < b < 1$, a mixed mechanism) [61]. To further separate the contributions of capacitive and diffusion processes, the

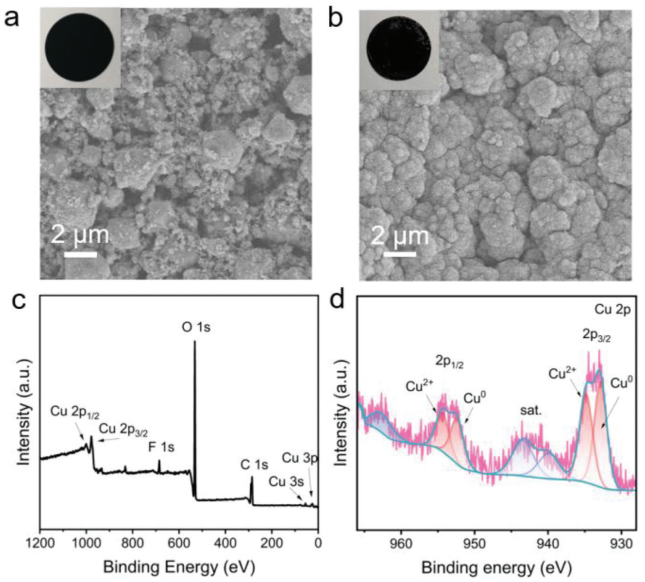

Fig. 5. SEM images of *quasi*-Cu-MOF composite (a) before and (b) after 400 cycles at 500 mA/g (inset: optical photo of the electrode sheets). (c) Full XPS survey spectrum of *quasi*-Cu-MOF composite. (d) XPS spectrum of Cu 2p.

contribution of diffusion and capacitance under particular potential voltages can be further calculated by Eq. 2 [62]:

$$i(\nu) = k_1\nu + k_2\nu^{1/2} \tag{2}$$

where both k_1 and k_2 are constants. In Eq. 2, $k_1\nu$ and $k_2\nu^{1/2}$ represent the contributions of the capacitance and diffusion processes, respectively. Therefore, the diffusion and capacitance contributions of M2 at different scan rates can be calculated and the shaded area (Fig. 4c and Fig. S5 in Supporting information) represents the capacitance contribution. As shown in Fig. 4d, for M2, with the scanning rate rising, capacitive contribution grows and the *pseudo*-capacitance-controlled electrochemical behaviour dominates by degree because the high specific surface area and abundant mesopores provide many sites for Li$^+$ ions transfer and storage [63,64].

The electrochemical impedance spectroscopy (EIS) of pristine Cu-MOF, M1, M2, and M3 was investigated before cycling, as shown in Fig. S6 (Supporting information). The fitting equivalent circuit was simulated (Table S2 in Supporting information), and the EIS consists of semicircles in the high-frequency region and oblique lines in the low-frequency zone, respectively reflecting the charge-transfer resistance (R_{ct}) and the Warburg impedance [65,66]. From these plots, the Rct value of M2 is 106.9 Ω, lower than that of pristine Cu-MOF (266.7 Ω), M1 (206.0 Ω) and M3 (151.1 Ω), indicating that M2 is more favourable of charge transfer during the cycling process. Compared with other samples, M2 has the largest slope in the low-frequency region, which proves that M2 is the best in ion diffusion [67]. Combined with the structure of materials, it is speculated that carbon and copper coating of M2 improves the conductivity of the cell for charge transfer, facilitating charge transmission from the lithium ions and electrons in the electrode [68,69]. In addition, the superior electrochemical performance of *quasi*-Cu-MOF composite is attributed to its 3D porous structure, which shortens the ion diffusion path, and this structure can release stress well to prevent stress concentration from damaging the material during charge and discharge.

To further study the stability of *quasi*-Cu-MOF composite, the structure and material changes of the active materials were observed by SEM (Fig. 5a) and XPS (Fig. 5c). Comparing the surface morphologies of the materials after cycling, it can be inferred that the introduction of an appropriate amount of copper (Fig. 5b) can effectively alleviate the volume expansion during cycling. However, the excessive copper precipitation is too rigid for the structure, resulting in the crushing of the structure (Fig. S7b in Supporting information). XPS results also show the characteristic peaks of Cu(II) (954.4 eV) and Cu^0 (952.4 eV). The Cu 2p signal after cycling is consistent with the characteristic peak positions before cycling (Fig. 5d). However, the intensity of characteristic peaks of Cu(II) and Cu^0 have changed, due to the reduction of the copper crystal phase in the electrochemical process. In addition, the C 1s spectrum in Fig. S8a (Supporting information) describes four main peaks centred at 289.7, 288.4, 285.8 and 284.8 eV, corresponding to C=O, O-C=O, C-O, C-C, respectively. In the O 1s spectrum (Fig. S8b in Supporting information), there are two peaks located at 532.0 and 531.6 eV, indexed to the C=O and Cu-O in *quasi*-Cu-MOF, respectively, which also proves the existence of copper particles without any kind of Cu_xO_y [70,71]. All the data indicated that M2 presents superior structural integrity during cycling, which is confirmed by its predominant cycling stability and the characterization of electrode materials.

In this work, the porous *quasi*-Cu-MOF composite was prepared by a facile one-step calcination method. The results show that the incomplete decomposition under low temperatures significantly affects the interaction between the copper nodes and the organic ligand in the composite. The *quasi*-Cu-MOF composite as LIB anodes showed superior long-term cycling performance (514.6 mAh/g at 500 mA/g after 400 cycles). Above superior performance is based on these aspects: the ultra-small size of copper nanoparticles restraining the volume expansion and preserving the structural integrity during cycling. The original MOF offers an intrinsic 3D structure for Li$^+$ storage performance. In addition, carbon and copper as conductive frameworks improve the conductivity. Furthermore, this work provides new insights for exploring high-efficiency electrode materials and helps rationally design *quasi*-MOF-based composite electrodes for energy storage and conversion.

Declaration of competing interest

The authors declare that they have no known competing financial interests or personal relationships that could have appeared to influence the work reported in this paper.

Acknowledgments

This work was supported by the National Natural Science Foundation of China (Nos. U1904215 and 21671170), the Top-notch Academic Programs Project of Jiangsu Higher Education Institutions (TAPP), Program for Young Changjiang Scholars of the Ministry of Education, China (No. Q2018270), and Natural Science Foundation of Jiangsu Province (No. BK20200044).

Supplementary materials

Supplementary material associated with this article can be found, in the online version, at doi:10.1016/j.cclet.2022.07.018.

References

[1] Y.S. Wei, M. Zhang, R. Zou, Q. Xu, Chem. Rev. 120 (2020) 12089–12174.
[2] X. Han, S. Wang, Y. Xu, et al., Energy Environ. Sci. 14 (2021) 5044–5056.
[3] L. Wang, T. Liu, T. Wu, J. Lu, Exploration 1 (2021) 20210130.
[4] S. Chuhadiya, Himanshu, D. Suthar, S.L. Patel, M.S. Dhaka, Coord. Chem. Rev. 446 (2021) 214115.
[5] M. Liu, N. Li, S. Cao, et al., Adv. Mater. 34 (2022) 2107421.
[6] Y. Gong, B. Shao, J. Mei, et al., Nano Res. 15 (2022) 551–556.
[7] G. Cai, P. Yan, L. Zhang, H.C. Zhou, H.L. Jiang, Chem. Rev. 121 (2021) 12278–12326.
[8] W. Dai, C. Kouvatas, W. Tai, et al., J. Am. Chem. Soc. 143 (2021) 1993–2004.

[9] M.D. Allendorf, V. Stavila, M. Witman, C.K. Brozek, C.H. Hendon, J. Am. Chem. Soc. 143 (2021) 6705–6723.
[10] Y. Chu, S. Xiong, Chin. Chem. Lett. 33 (2022) 486–490.
[11] M. Xu, D. Li, K. Sun, et al., Angew. Chem. Int. Ed. 60 (2021) 16372–16376.
[12] Y. Bai, C. Liu, T. Chen, et al., Angew. Chem. Int. Ed. 60 (2021) 25318–25322.
[13] Q. Zhao, X. Chen, W. Hou, et al., SusMat 2 (2022) 104–112.
[14] H. Yang, W. Cui, Y. Han, B. Wang, Chin. Chem. Lett. 29 (2018) 842–844.
[15] Y. Wang, H. Jin, Q. Ma, et al., Angew. Chem. Int. Ed. 59 (2020) 4365–4369.
[16] J. Zhai, Q. Kang, Q. Liu, et al., J. Colloid Interface Sci. 608 (2022) 1942–1950.
[17] M. Bagheri, A. Melillo, B. Ferrer, M.Y. Masoomi, H. Garcia, ACS Appl. Mater. Interfaces 14 (2022) 978–989.
[18] Y.Y. Hu, R.X. Han, L. Mei, et al., Mater. Today Energy 19 (2021) 100608.
[19] M. Bagheri, M.Y. Masoomi, E. Domínguez, H. García, ACS Sustain. Chem. Eng. 9 (2021) 10611–10619.
[20] J. Zhang, Y. Wang, H. Wang, D. Zhong, T. Lu, Chin. Chem. Lett. 33 (2022) 2065–2068.
[21] N. Tsumori, L. Chen, Q. Wang, et al., Chem 4 (2018) 845–856.
[22] M. Bagheri, A. Melillo, B. Ferrer, M.Y. Masoomi, H. Garcia, Chemistry 27 (2021) 14273–14281 (Easton).
[23] M. Bagheri, M.Y. Masoomi, A. Forneli, H. García, J. Phys. Chem. C 126 (2021) 683–692.
[24] Y. Wu, Y. Li, J. Gao, Q. Zhang, SusMat 1 (2021) 66–87.
[25] W.G. Cui, Y.T. Li, H. Zhang, et al., Appl. Catal. B 278 (2020) 119262.
[26] L. Ai, N. Li, M. Chen, H. Jiang, J. Jiang, J. Mater. Chem. A 9 (2021) 16479–16488.
[27] Y. Shen, L. Bao, F. Sun, T. Hu, Mater. Chem. Front. 3 (2019) 2363–2373.
[28] L. Fan, F. Zhao, Z. Huang, et al., Appl. Catal. A 572 (2019) 34–43.
[29] T. Wang, H. Zhu, Q. Zeng, D. Liu, Adv. Mater. Interfaces 6 (2019) 1900423.
[30] K. Wang, C. Wu, F. Wang, N. Jing, G. Jiang, ACS Sustain. Chem. Eng. 7 (2019) 18582–18592.
[31] H. Xia, N. Li, W. Huang, Y. Song, Y. Jiang, ACS Appl. Mater. Interfaces 13 (2021) 22240–22253.
[32] C. Arul, K. Moulaee, N. Donato, et al., Sens. Actuator B 329 (2021) 129053.
[33] G. Zheng, Z. Xing, X. Gao, et al., Appl. Surf. Sci. 559 (2021) 149701.
[34] L. Zhu, Z. Yao, T. Liu, et al., Chem. Commun. 56 (2020) 5847–5850.
[35] W. Liu, Z. Zhang, Y. Zhang, et al., Nano Micro Lett. 13 (2021) 61.
[36] L. Zhu, Z. Yao, T. Liu, et al., Chem. Commun. 56 (2020) 5847–5850.
[37] X. Cai, Z. Xie, M. Pang, J. Lin, Cryst. Growth Des. 19 (2019) 556–561.
[38] S. Shang, Z. Tao, C. Yang, et al., Chem. Eng. J. 393 (2020) 124666.
[39] D.H. Nam, O.S. Bushuyev, J. Li, et al., J. Am. Chem. Soc. 140 (2018) 11378–11386.
[40] H. Qing, R. Wang, Z. Chen, et al., J. Colloid Interface Sci. 566 (2020) 1–10.
[41] A. Rendón-Calle, Q.H. Low, S.H.L. Hong, et al., Appl. Catal. B 285 (2021) 119776.
[42] Z. Li, D. Wang, W. Wei, et al., Solid State Sci. 108 (2020) 106375.
[43] R. Yun, B. Zhang, F. Zhan, et al., Inorg. Chem. 60 (2021) 12906–12911.
[44] J. Yan, H. Wang, B. Jin, M. Zeng, R. Peng, J. Solid State Chem. 297 (2021) 122060.
[45] R. Wei, Y. Dong, Y. Zhang, et al., J. Colloid Interface Sci. 582 (2021) 236–245.
[46] P. Hu, A. Yuan, C. Meng, H. Chen, H. Zhou, ChemElectroChem 7 (2020) 4003–4009.
[47] J. Yan, Y. Cui, M. Xie, et al., Angew. Chem. Int. Ed. 60 (2021) 24467–24472.
[48] X. Lou, X. Hu, S. Xiang, et al., New J. Chem. 44 (2020) 17899–17905.
[49] S. Maiti, A. Pramanik, U. Manju, S. Mahanty, Microporous Mesoporous Mater. 226 (2016) 353–359.
[50] Q. Gan, H. He, K. Zhao, Z. He, S. Liu, J. Colloid Interface Sci. 530 (2018) 127–136.
[51] T. Gong, X. Lou, E.Q. Gao, B. Hu, ACS Appl. Mater. Interfaces 9 (2017) 21839–21847.
[52] J. Qiu, M. Yu, Z. Zhang, X. Cai, G. Guo, J. Alloys Compd. 775 (2019) 366–371.
[53] Y.G. Weng, Z.H. Ren, Z.R. Zhang, et al., Inorg. Chem. 60 (2021) 17074–17082.
[54] D. Ge, J. Peng, G. Qu, et al., New J. Chem. 40 (2016) 9238–9244.
[55] X. Zhang, H. Liu, L. Jiang, Adv. Mater. 31 (2019) e1804508.
[56] Q. Zhang, Q. Gao, W. Qian, et al., Mater. Today Energy 13 (2019) 93–99.
[57] L. Du, Q. Wu, L. Yang, et al., Nano Energy 57 (2019) 34–40.
[58] Q. Cheng, S. Han, K. Mao, et al., Nano Energy 52 (2018) 485–493.
[59] S. Wu, G. Fu, W. Lv, et al., Small 14 (2018) 1702667.
[60] L. Jiao, J. Zhu, Y. Zhang, et al., J. Am. Chem. Soc. 143 (2021) 19417–19424.
[61] L. Fan, X. Guo, W. Li, X. Hang, H. Pang, Chin. Chem. Lett. 34 (2023) 107447.
[62] K. Amin, J. Zhang, H. Zhou, et al., Sustain. Energy Fuels 4 (2020) 4179–4185.
[63] W. Zhao, L. Gao, L. Yue, et al., J. Mater. Chem. A 9 (2021) 6402–6412.
[64] H. Li, T. Wei, S. Huang, et al., New J. Chem. 45 (2021) 12168–12177.
[65] J. Kim, W. Jang, J.H. Kim, C. Yang, Compos. B. Eng. 222 (2021) 109083.
[66] N. Li, Y. Liu, X. Ji, et al., Chin. Chem. Lett. 32 (2021) 3787–3792.
[67] X. Jiao, Y. Liu, T. Li, et al., ACS Appl. Mater. Interfaces 11 (2019) 30858–30864.
[68] Q. Feng, T. Li, Y. Miao, et al., J. Colloid Interface Sci. 608 (2022) 227–238.
[69] X. Shi, J. Yu, Q. Liu, et al., Sustain. Mater. Technol. 28 (2021) e00275.
[70] W. Xu, W. Li, H. Wen, et al., Appl. Catal. B 286 (2021) 119946.
[71] X. Li, H. Liu, X. Jia, et al., Sci. Total Environ. 621 (2018) 1533–1541.